Nano Research

ISSN 1998-0124 CN 11-5974/O4
https://doi.org/10.1007/s12274-019-2483-8

Research Article

In situ TEM observation of neck formation during oriented attachment of PbSe nanocrystals

Yu Wang[1,2], Xinxing Peng[1,3], Alex Abelson[4], Bing-Kai Zhang[1], Caroline Qian[4], Peter Ercius[5], Lin-Wang Wang[1], Matt Law[4], and Haimei Zheng[1,2] (✉)

[1] *Materials Sciences Division, Lawrence Berkeley National Laboratory, Berkeley, California 94720, USA*
[2] *Department of Materials Science and Engineering, University of California, Berkeley, California 94720, USA*
[3] *State Key Lab of Physical Chemistry of Solid Surfaces, Collaborative Innovation Center of Chemistry for Energy Materials, College of Chemistry and Chemical Engineering, Xiamen University, Xiamen 361005, China*
[4] *Department of Chemistry, University of California, Irvine, California 92697, USA*
[5] *National Center for Electron Microscopy, Molecular Foundry, Lawrence Berkeley National Laboratory, Berkeley, California 94720, USA*

Received: 16 May 2019 / **Revised:** 11 July 2019 / **Accepted:** 16 July 2019

ABSTRACT

Oriented attachment of nanocrystals is an important route to constructing epitaxially-connected nanocrystal superlattices for various applications. During oriented attachment of semiconductor nanocrystals, neck can be formed between nanocrystals and it strongly influences the properties of the resulting superlattice. However, the neck formation mechanism is poorly understood. Here, we use *in situ* liquid cell transmission electron microscopy to directly observe the nucleation and growth of homoepitaxial necks between PbSe nanocrystals with atomic details. We find that neck initiation occurs slowly (~ 10 s) when two nanocrystals approach to each other within an edge-to-edge distance of 0.6 nm. During neck initiation, Pb and Se atoms defuse from other facets into the gap, forming "dynamic reversible" filaments. Once the filament (neck) width is larger than a critical size of 0.9 nm, it gradually (15 s) widens into a 3-nm-wide neck. The atomic structure of the neck is further obtained using *ex situ* aberration-corrected scanning TEM imaging. Neck initiation and growth mechanisms are elucidated with density functional theory calculations. Our direct unveiling of the atomic pathways of neck formation during oriented attachment shed light into the fabrication of nanocrystal superlattices with improved structural order and electronic properties.

KEYWORDS

PbSe nanocrystals, quantum dots, superlattices, necking, oriented attachment, liquid cell TEM

1 Introduction

Oriented attachment of colloidal nanocrystals occurs in a variety of natural and synthetic systems [1, 2], in which nanocrystals connect preferentially along specific crystal facets to form a single crystal. During oriented attachment, the inter-nanocrystal connection, which is achieved through a "necking" process [3–6], is essential for regulating the coherent coupling effects in superlattices [7, 8] and thus enabling the emergence of various novel properties [7, 9, 10]. For instance, epitaxially-connected superlattices of semiconductor nanocrystals may show remarkable electronic phenomena including topological states and Dirac cones [11–13]. These phenomena will be favored in superlattices with atomically-uniform inter-nanocrystal necks that increase the electron delocalization length [14, 15]. To understand necking in nanocrystal superlattices, recent efforts have used X-ray scattering [16–18] and *ex situ* TEM [19–21] to characterize the superlattice structure before and after oriented attachment. These measurements indicate that the center-to-center distance of epitaxially-connected nanocrystals is often larger than the diameter of the initial nanocrystals [12, 22]. It has been presumed that necking may be achieved through a "click and cascade" model when two nanocrystals are at a short range and separated by solvent molecules [22]. However, the mechanism of neck formation in nanocrystal superlattices is unclear due to the lack of direct observation [23–26]. Elucidating the mechanism(s) of nanocrystal necking is significant not only for interpreting semiconductor crystallization through particle attachment [27], but also for improving the inter-nanocrystal connectivity in nanocrystal superlattices to achieve novel electronic properties [14, 28].

Here, we report real-time atomic-resolution imaging of the necking process during oriented attachment of PbSe nanocrystals by liquid-phase TEM [29–32]. During the superlattice transformation from quasi-hexagonal oleate-capped PbSe nanocrystal monolayers to quasi-square epitaxially-connected nanocrystal monolayers, we find that the necking occurs in three stages: (i) nanocrystals first approach each other and the lattice angle changes from ~ 60° to ~ 90°, indicating a geometry change from hexagonal to square; (ii) When the neighboring nanocrystals reach a gap (surface-to-surface) distance of ~ 0.6 nm due to the separation of ligand residuals, they stop moving and start building a neck. Atom-resolved imaging shows that it takes 5–10 s to form a stable neck nucleus with a critical size of 0.6 nm × 0.9 nm (neck length and width); (iii) After initiation, the neck grows to 3 nm in width in ~15 s. Using *ex situ* scanning TEM, we confirm the formation of two-atom-long necks during the superlattice phase transition. The mechanism of neck initiation and growth is rationalized with density functional theory (DFT) calculations.

Address correspondence to hmzheng@lbl.gov

2 Results and discussion

We formed hexagonal self-assembled monolayers of oleate-capped PbSe nanocrystals (6.2 nm diameter) by drop-casting 4 μL of a 0.5 mg/mL hexane suspension of the nanocrystals onto a 10-nm thick carbon-film TEM grid. We then deposited 100 nL of anhydrous ethylene glycol (EG) on a second TEM grid and sandwiched the two grids together to form a carbon-film liquid cell for *in situ* TEM imaging. The fluctuation of EG during *in situ* imaging initiates the oriented attachment of PbSe nanocrystals, enabling real-time imaging of the necking process with atomic resolution (Movies ESM1–ESM4).

The image series in Fig. 1(a) and Movie ESM1 depict the oriented attachment of six nanocrystals (**1** to **6**). At 0 s, nanocrystals **2** and **3** are already connected, whereas the other nanocrystals are discrete in a quasi-hexagonal geometry. Over the next 50 s, the nanocrystals move towards their neighboring nanocrystals and fuse into a quasi-square superlattice. The trajectory of each nanocrystal center and the inter-nanocrystal connectivity are shown in Fig. 1(b), from which we analyze the change of four representative lattice angles (α–δ). As shown in Fig. 1(c), all four lattice angles increase from ~ 60° towards 90°, indicating the superlattice symmetry changes from hexagonal to square as the nanocrystals approach each other.

The change of gap distances (distance between the nanocrystal surfaces) between five initially unconnected nanocrystal pairs is plotted in Fig. 1(d). nanocrystals **1** and **2** (a representative pair) approach each other from a gap distance of 4.5 nm at 0 s with a speed of ~ 0.3 nm·s^{-1}. The approach speed gradually decreases and translational motion stops at a distance of 0.6 nm at 21 s. As shown in the third image in Fig. 1(a) (20.0 s), there is still a clear gap between nanocrystals **1** and **2** at this time.

It takes an additional ~ 10 s to build a discernible neck, which we consider the onset of neck initiation. Although other nanocrystal pairs have different initial gap distances and different approach speeds, all nanocrystal pairs were observed to follow the same three-stage oriented attachment process (Fig. 1(d)): (i) the nanocrystals move to within ~ 0.6 nm of each other, (ii) a neck nucleus forms after 5–10 s, and (iii) the neck widens until it becomes a stable size. Additional examples of this three-stage oriented attachment process can be found in Movies ESM2 and ESM3, which are analyzed in Figs. S1 and S2 in the Electronic Supplementary Material (ESM) and show a very similar final gap distance (~ 0.6 nm) and neck initiation time (5–10 s).

The atomistic pathway of neck initiation and growth is explored in Movie ESM4 and Fig. 2(a). The clear lattice fringes visible throughout the movie enable us to reconstruct atomic models of neck initiation and growth (right column in Fig. 2(a)). We find that nanocrystals align in a same <100> axial occurs before neck initiation. In the first image (2.0 s), the two unconnected nanocrystals are separated by 0.6 nm and show biaxially-aligned {200} planes perpendicular to the inter-nanocrystal axis. The *d*-spacing of the {200} planes remains constant at ~ 3.1 Å during neck formation, indicating the absence of strong lattice distortion. By counting the {200} planes, we find that both nanocrystals initially have 20 atomic layers along the inter-nanocrystal direction, and after the oriented attachment, two extra {200} layers form in the 0.6 nm gap. As reflected by the edge trajectories of nanocrystals (Fig. 2(b)), the nanocrystal centers barely change position during the necking process, whereas the nanocrystal width (perpendicular to inter-nanocrystal direction) decreases slightly as the neck grows. This suggests that the necks grow as surface atoms on the lateral facets of the nanocrystals diffuse into the inter-nanocrystal regions. Note that, there is a slight increase in the length of the left nanocrystal in Fig. 2(b) during the later stage of neck growth, which is probably caused by the deformability of PbSe nanocrystals after the removal of capped ligands. Recently, we have reported that the deformability of PbSe nanocrystals is strongly dependent on the kinetics of ligand removal [33], e.g., fast ligand removal by ethylenediamine solution induces drastic elongation of nanocrystals along inter-nanocrystal direction, whereas slow ligand removal by EG (same condition used in the current work) leads to reduced deformability of nanocrystals. The driving force of nanocrystal deformation is ascribed to the dipole interaction between nanocrystals based on comparison experiments and molecular dynamics simulations [20, 33, 34].Closer scrutiny of the *in situ* movies reveals that neck initiation involves the formation of transient atomic PbSe filaments (e.g., see image at 3.0 s) prior to the appearance of a stable neck nucleus. Fig. 2(c) shows a time trace of the filament/neck width. We find that the width fluctuates between 0–0.9 nm from 2 to 7 s due to the formation and cleavage of thin PbSe filaments. Eventually, a

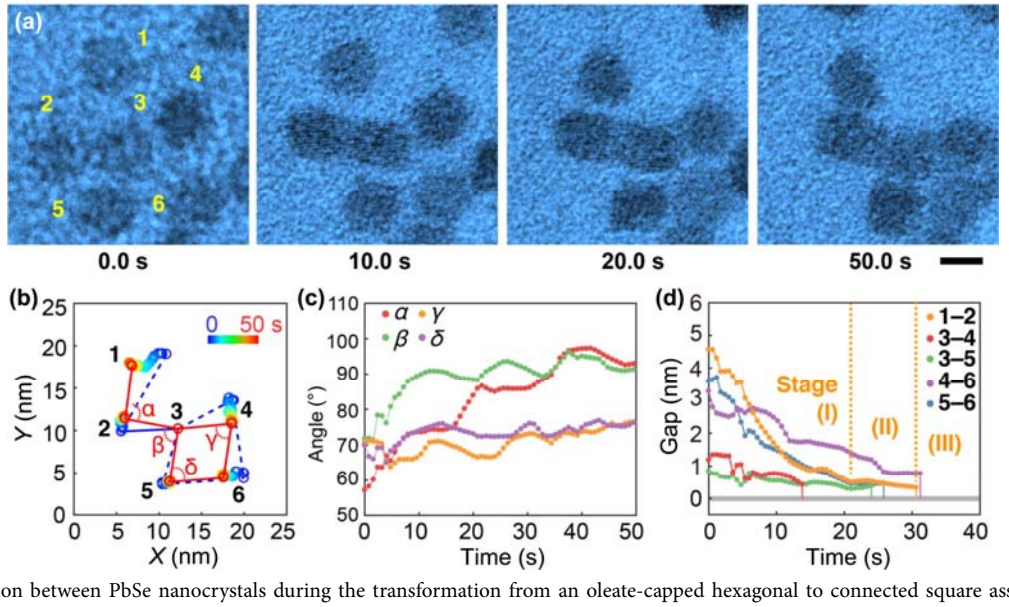

Figure 1 Neck formation between PbSe nanocrystals during the transformation from an oleate-capped hexagonal to connected square assembly. (a) Sequence of *in situ* TEM images showing the translational motion and necking of six nanocrystals. Images are extracted from Movie S1 and shown in false color. Scale bar, 5 nm. (b) Trajectories of the nanocrystal centers showing the transformation from the hexagonal to square geometry. Dashed and solid lines denote nanocrystal pairs that are unconnected or connected, respectively. Four inter-nanocrystal angles are labeled α–δ. (c) Plot of the four angles versus time. (d) Time trace of the gap distances of six nanocrystal pairs showing the three-stage necking pathway. Pair **1**–**2** (orange dots and lines) highlights the three stages of neck formation: (I) approach, (II) arrest and neck nucleation, and (III) neck growth. When the trace falls to the gray bar (0 nm), it denotes a stable nucleus formed between the nanocrystal pair.

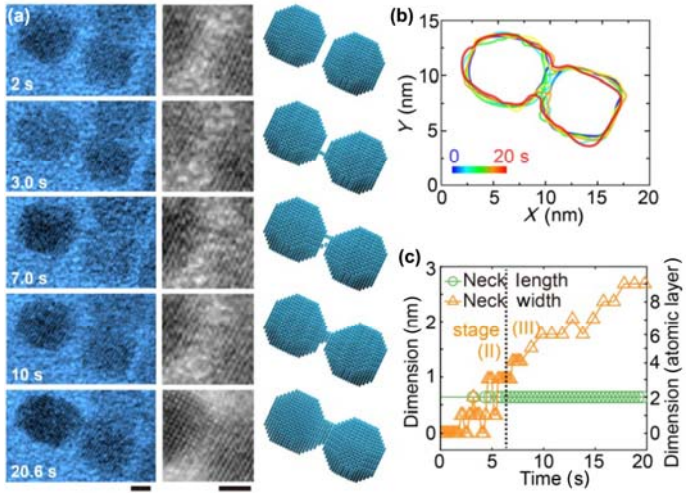

Figure 2 Atomistic pathway of neck nucleation between two PbSe nanocrystals. (a) Representative sequence of *in situ* TEM images (left column) extracted from Movie ESM4, magnified views (middle column) and atomic models (right column) showing the necking details. Only Pb atoms are shown in models for clarity and a closer comparison to TEM images. Both scale bars are 2 nm. (b) Trajectories of the nanocrystal edges showing the nanocrystal shape change during neck formation. (c) Time trace of the neck length and width during the neck nucleation and growth stages (separated by dashed vertical line).

stable nucleus with a width of > 0.9 nm forms and grows to ~ 2.7 nm in width in 20 s. Meanwhile, the neck length is fixed at 0.6 nm (the final gap distance).

We employed *ex situ* high-angle annular dark field scanning TEM (HAADF-STEM) imaging to investigate neck formation in large-area superlattices. We performed the superlattice transformation with a similar procedure to the one used *in situ*, i.e., first forming a hexagonal monolayer on a carbon-film TEM grid, then immersing the grid in anhydrous EG for 30 s to trigger the oriented attachment. The large-area structures are characterized before and after EG treatment by HAADF-STEM and analyzed using custom computer vision scripts (Figs. 3(a)–3(e) and Fig. S3 in the ESM). We observe that nanocrystals are mostly epitaxially connected in the square superlattice (Fig. S4 in the ESM) and the center-to-center distance of adjacent nanocrystals is larger than the initial nanocrystal diameter, in accord with our *in situ* results and previous reports of square superlattices prepared by nanocrystal self-assembly on the surface of EG [12, 33]. We note that the precise neck length should not be directly calculated as the difference between center-to-center distance and nanocrystal diameter; instead, it should be calculated as difference between center-to-center distance and the nanocrystal size along <100> directions. A precondition for obtaining monodisperse necks is the use of monodisperse nanocrystals. Statistical analysis of several images shows that nanocrystals in the hexagonal monolayer are highly monodisperse, with 95% of the nanocrystals having a diameter of 6.2 ± 0.1 nm (Figs. 3(a) and 3(c)). These nanocrystals contain 20 atomic layers in the <100> directions, which is consistent with the nanocrystal size measured in Fig. 2. After EG treatment, a square superlattice forms (Fig. 3(b)) with an average center-to-center distance of 6.7 nm (Fig. 3(d)). Therefore, the neck length is calculated as the difference between the center-to-center distance (6.7 nm) and the nanocrystal size along the <100> directions (20 atomic layers, 6.1 nm). In addition, Fig. 3(e) shows the histogram of neck width, indicating an average width of 3.0 nm, comparable to the neck width measured *in situ* at 20 s (Fig. 2).

We confirmed an average neck length of two atomic layers by *ex situ* atomic-resolution imaging (Figs. 3(f) and 3(g)). The associated fast Fourier transform (FFT, Fig. 3(f) inset) shows the uniform oriented attachment in the connected superlattice. The overlaid boxes with a size of 20 × 20 atomic layers help to visualize the necks and determine their length (Fig. 3(g)). Most of the necks are two atomic layers long (Fig. 3(h)).

Previous studies on gold crystallization found that oriented attachment of gold nanocrystals may also involve the necking of nanoparticles with a gap distance of ~ 0.5 nm [35, 36]. It was proposed that the gold nanocrystals stop at the small gap distance because of the separation of solvent, i.e., water [37]. Our recent atomic-resolution *in situ* TEM study on gold nanocrystals suggests the ligands could play an important role in separating gold nanocrystals during oriented attachment [38]. We have observed that the approaching PbSe nanocrystals stop at a gap distance of 0.6 nm before the neck initiation in EG, and we speculate that this is resulted from the ligand-enforced separation of nanocrystals. Because the EG treatment is not good at removing oleate ligands as other strong ligand-removal agents such as ethylenediamine (EDA) [39]. Most of the oleate remains bound after EG treatment, but the {100} facets have a much lower oleate coverage than the other facets since the binding energy is low. The residual bound oleate can move and flex and might be compressed to lie along the {100} surface, which stops the dots at ~ 0.6 nm. As the atoms begin filling in the gap, it displaces the oleate ligands, pushing them out to the periphery of the neck or onto the other facets.

We performed a comparison experiment on the oriented attachment of PbSe nanocrystals in the presence of strong ligand-removal agent EDA, and found that when the oleate ligands were aggressively removed by EDA, the nanocrystals attached directly without showing the separation stage (Movie ESM5 and Fig. S5 in the ESM). This suggests that the separation of nanocrystals before neck initiation is more likely caused by oleate ligands rather than EG solvents.

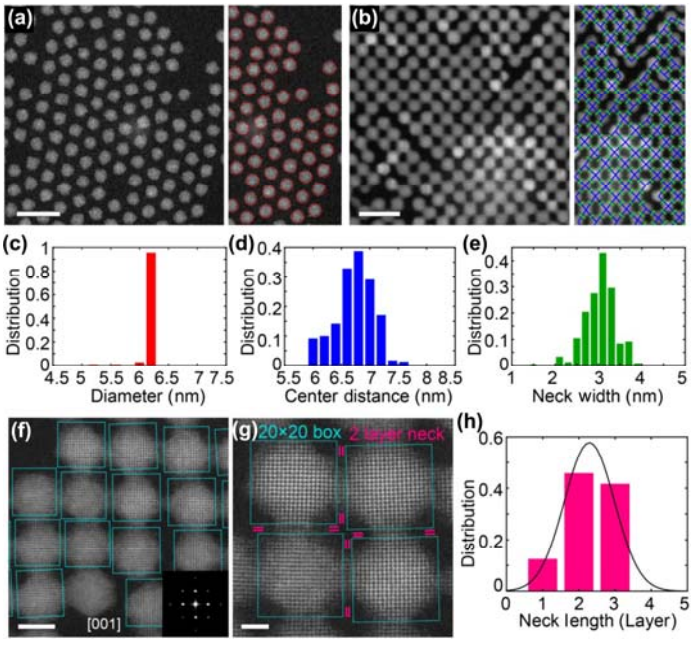

Figure 3 *Ex situ* HAADF-STEM characterization of neck structure in large-area superlattices. (a) and (b) HAADF-STEM images of a hexagonal oleate-capped nanocrystal monolayer and an epitaxially-connected square superlattice. Right columns show the nanocrystal diameter (red circles), center-to-center distance (blue lines), and neck width (green lines) in half of each image as determined by computer vision (Fig. S3 in the ESM). (c) Histogram showing the distribution of nanocrystal diameter in the hexagonal monolayer in (a). (d) and (e) Histograms showing the distribution of center-to-center distance and neck width in the square superlattice in (b). (f) Atomic-resolution image and fast Fourier transform image (inset) showing the uniform nanocrystal orientation and neck connectivity in the square superlattice. Cyan boxes with a size of 20 × 20 Pb layers help to visualize the neck lengths. (g) Magnified image of several necks that are two Pb layers (0.6 nm) long. (h) Histogram of neck length obtained by counting the extra Pb layers between nanocrystals as indicated in (g). Scale bars are 20 nm in (a) and (b), 5 nm in (f), and 2 nm in (g).

We performed DFT calculations to test the hypothesis of ligand-enforced separation and better understand the necking mechanism. In order to reduce the calculation time while retaining the main structures of oleate ligands and PbSe nanocrystals, we simulated the structure with an oleic acid fragment (the alkyl tail after the alkene group omitted) sandwiched between the {001} facets of two rock salt PbSe crystals (Fig. 4(a)). With decreasing gap distance, the system energy first decreases and then increases as the ligand is sterically confined within the inter-nanocrystal gap. The system energy is minimized at a gap distance of 0.55–0.8 nm, in accord with the final gap distance observed with *in situ* and *ex situ* TEM imaging.

We further evaluate the critical nucleus size by adding pairs of Pb and Se atoms into the 0.6 nm gap (Fig. 4(c)). The energy change ΔE by moving atoms from bulk crystal into the neck is calculated as $\Delta E = E_{necked} - (E_{double\text{-}slab} + n \times E_{bulk})$. Note that, in reality, the atoms for forming neck are most likely from the edge or surface of nanocrystals, which have higher energy than that of bulk crystals. Therefore, the calculated ΔE does not represent the energy barrier of neck formation directly, instead, it provides the relative energy comparison of the structures with different neck thickness, which is important to show the different stability of filaments and thick necks. As shown in Fig. 4(d), when adding the first 9 pairs of Pb and Se atoms, ΔE generally increases with considerable fluctuations caused by surface energy change. Upon further addition of Pb and Se atoms, ΔE decreases and the fluctuations cease, indicating the existence of an energy barrier and critical size for neck initiation and growth. The critical nucleus contains 9 pairs of Pb and Se atoms, which is two atoms long and 3 × 3 atoms thick, i.e., 0.9 nm in width. We note that this size is consistent with the *in situ* observation of neck formation in Fig. 2.

We reported *in situ* observation of neck formation of semiconductor nanocrystals in liquid phase. We show that neck formation between PbSe nanocrystals occurs in three stages: (i) nanocrystals approach each other and stop at a distance of 0.6 nm, separated by a low coverage of residual oleate ligands; (ii) a stable neck nucleates after a period of transient atomic filament formation; (iii) the neck increases in width at a fixed length, supplied by surface atoms from neighboring facets. We provide basic kinetic data (e.g., initiation time) and critical spatial information (e.g., gap distance and critical nucleus size) that can only be obtained through *in situ* investigations. We confirm the neck size by the statistics of *ex situ* formed large-area superlattices with atomic precision. We also elucidate the initiation and growth mechanisms by DFT calculations. By revealing the necking phenomenon in unprecedented atomic detail, this study provides critical insights into how individual nanocrystals transform into epitaxially connected superlattices. Our improved understanding of neck initiation and growth will facilitate the fabrication of epitaxially-connected nanocrystal superlattices with better neck connectivity and uniformity, which may prove essential for achieving mini-band transport in these materials.

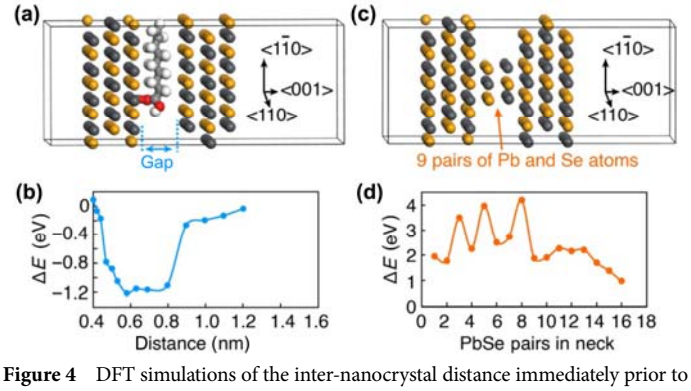

Figure 4 DFT simulations of the inter-nanocrystal distance immediately prior to neck formation and the critical neck thickness during neck nucleation. (a) Sandwich structure with an oleic acid fragment between the {001} surfaces of two rock salt PbSe crystals. (b) The change of system energy as a function of gap distance. (c) Relaxed structure of two {001} surfaces with a neck consisting of nine pairs of Pb and Se atoms arranged in a 3 × 3 × 2 cuboid. (d) ΔE change as moving different pairs of Pb and Se atoms from bulk into the gap, showing the instability of thin filaments with few atom pairs and the increased stability of necks with more than 9 atom pairs.

Acknowledgements

This work was supported by the U.S. Department of Energy (DOE), Office of Science, Office of Basic Energy Sciences (BES), Materials Sciences and Engineering Division under Contract No. DE-AC02-05-CH11231 within the *in-situ* TEM (KC22ZH) program. Y. W., A. A., C. Q., and M. L. were supported by the UC Office of the President under the UC Laboratory Fees Research Program Collaborative Research and Training Award LFR-17-477148. X. P. acknowledges financial support from the China Scholarship Council. Work at the Molecular Foundry was supported by the Office of Science, Office of Basic Energy Sciences, of the U.S. Department of Energy under Contract No. DE-AC02-05CH11231.

Electronic Supplementary Material: Supplementary material (e.g. additional *in situ* movie analysis, STEM imaging, image processing method, and calculation method) is available in the online version of this article at https://doi.org/10.1007/s12274-019-2483-8.

References

[1] Zhang, X.; Shen, Z.; Liu, J.; Kerisit, S. N.; Bowden, M. E.; Sushko, M. L.; De Yoreo, J. J.; Rosso, K. M. Direction-specific interaction forces underlying zinc oxide crystal growth by oriented attachment. *Nat. Commun.* **2017**, *8*, 835.

[2] Li, D. S.; Nielsen, M. H.; Lee, J. R. I.; Frandsen, C.; Banfield, J. F.; De Yoreo, J. J. Direction-specific interactions control crystal growth by oriented attachment. *Science* **2012**, *336*, 1014–1018.

[3] Whitham, K.; Smilgies, D. M.; Hanrath, T. Entropic, enthalpic, and kinetic aspects of interfacial nanocrystal superlattice assembly and attachment. *Chem. Mater.* **2018**, *30*, 54–63.

[4] Sandeep, C. S. S.; Azpiroz, J. M.; Evers, W. H.; Boehme, S. C.; Moreels, I.; Kinge, S.; Siebbeles, L. D. A.; Infante, I.; Houtepen, A. J. Epitaxially connected PbSe quantum-dot films: Controlled neck formation and optoelectronic properties. *ACS Nano* **2014**, *8*, 11499–11511.

[5] Lim, T. H.; McCarthy, D.; Hendy, S. C.; Stevens, K. J.; Brown, S. A.; Tilley, R. D. Real-time TEM and kinetic monte carlo studies of the coalescence of decahedral gold nanoparticles. *ACS Nano* **2009**, *3*, 3809–3813.

[6] Simon, P.; Bahrig, L.; Baburin, I. A.; Formanek, P.; Röder, F.; Sickmann, J.; Hickey, S. G.; Eychmuller, A.; Lichte, H.; Kniep, R. et al. Interconnection of nanoparticles within 2D superlattices of PbS/oleic acid thin films. *Adv. Mater.* **2014**, *26*, 3042–3049.

[7] Whitham, K.; Hanrath, T. Formation of epitaxially connected quantum dot solids: Nucleation and coherent phase transition. *J. Phys. Chem. Lett.* **2017**, *8*, 2623–2628.

[8] Xu, Y. H.; Wang, X. X.; Zhang, W. L.; Lv, F.; Guo, S. J. Recent progress in two-dimensional inorganic quantum dots. *Chem. Soc. Rev.* **2018**, *47*, 586–625.

[9] Talapin, D. V.; Lee, J. S.; Kovalenko, M. V.; Shevchenko, E. V. Prospects of colloidal nanocrystals for electronic and optoelectronic applications. *Chem. Rev.* **2010**, *110*, 389–458.

[10] Boles, M. A.; Engel, M.; Talapin, D. V. Self-assembly of colloidal nanocrystals: From intricate structures to functional materials. *Chem. Rev.* **2016**, *116*, 11220–11289.

[11] Kagan, C. R.; Lifshitz, E.; Sargent, E. H.; Talapin, D. V. Building devices from colloidal quantum dots. *Science* **2016**, *353*, aac5523.

[12] Boneschanscher, M. P.; Evers, W. H.; Geuchies, J. J.; Altantzis, T.; Goris, B.; Rabouw, F. T.; van Rossum, S. A. P.; van der Zant, H. S. J.; Siebbeles, L. D. A.; van Tendeloo, G. et al. Long-range orientation and atomic attachment of nanocrystals in 2D honeycomb superlattices. *Science* **2014**, *344*, 1377–1380.

[13] Beugeling, W.; Kalesaki, E.; Delerue, C.; Niquet, Y. M.; Vanmaekelbergh, D.; Smith, C. M. Topological states in multi-orbital HgTe honeycomb lattices. *Nat. Commun.* **2015**, *6*, 6316.

[14] Whitham, K.; Yang, J.; Savitzky, B. H.; Kourkoutis, L. F.; Wise, F.; Hanrath, T. Charge transport and localization in atomically coherent quantum dot solids. *Nat. Mater.* **2016**, *15*, 557–563.
[15] Evers, W. H.; Schins, J. M.; Aerts, M.; Kulkarni, A.; Capiod, P.; Berthe, M.; Grandidier, B.; Delerue, C.; van der Zant, H. S. J.; van Overbeek, C. et al. High charge mobility in two-dimensional percolative networks of PbSe quantum dots connected by atomic bonds. *Nat. Commun.* **2015**, *6*, 8195.
[16] Geuchies, J. J.; van Overbeek, C.; Evers, W. H.; Goris, B.; de Backer, A.; Gantapara, A. P.; Rabouw, F. T.; Hilhorst, J.; Peters, J. L.; Konovalov, O. et al. *In situ* study of the formation mechanism of two-dimensional superlattices from PbSe nanocrystals. *Nat. Mater.* **2016**, *15*, 1248–1254.
[17] Weidman, M. C.; Smilgies, D. M.; Tisdale, W. A. Kinetics of the self-assembly of nanocrystal superlattices measured by real-time *in situ* X-ray scattering. *Nat. Mater.* **2016**, *15*, 775–781.
[18] Zaluzhnyy, I. A.; Kurta, R. P.; Andre, A.; Gorobtsov, O. Y.; Rose, M.; Skopintsev, P.; Besedin, I.; Zozulya, A. V.; Sprung, M.; Schreiber, F. et al. Quantifying angular correlations between the atomic lattice and the superlattice of nanocrystals assembled with directional linking. *Nano Lett.* **2017**, *17*, 3511–3517.
[19] Yalcin, A. O.; Fan, Z. C.; Goris, B.; Li, W. F.; Koster, R. S.; Fang, C. M.; van Blaaderen, A.; Casavola, M.; Tichelaar, F. D.; Bals, S. et al. Atomic resolution monitoring of cation exchange in CdSe-PbSe heteronanocrystals during epitaxial solid-solid-vapor growth. *Nano Lett.* **2014**, *14*, 3661–3667.
[20] Cho, K. S.; Talapin, D. V.; Gaschler, W.; Murray, C. B. Designing PbSe nanowires and nanorings through oriented attachment of nanoparticles. *J. Am. Chem. Soc.* **2005**, *127*, 7140–7147.
[21] Evers, W. H.; Goris, B.; Bals, S.; Casavola, M.; de Graaf, J.; van Roij, J.; Dijkstra, M.; Vanmaekelbergh, D. Low-dimensional semiconductor superlattices formed by geometric control over nanocrystal attachment. *Nano Lett.* **2013**, *13*, 2317–2323.
[22] van Overbeek, C.; Peters, J. L.; van Rossum, S. A. P.; Smits, M.; van Huis, M. A.; Vanmaekelbergh, D. Interfacial self-assembly and oriented attachment in the family of PbX (X = S, Se, Te) nanocrystals. *J. Phys. Chem. C* **2018**, *122*, 12464–12473.
[23] Tan, S. F.; Chee, S. W.; Lin, G. H.; Mirsaidov, U. Direct observation of interactions between nanoparticles and nanoparticle self-assembly in solution. *Acc. Chem. Res.* **2017**, *50*, 1303–1312.
[24] Qi, K.; Wei, J. K.; Sun, M. H.; Huang, Q. M.; Li, X. M.; Xu, Z.; Wang, W. L.; Bai, X. D. Real-time observation of deep lithiation of tungsten oxide nanowires by *in situ* electron microscopy. *Angew. Chem., Int. Ed.* **2015**, *127*, 15437–15440.
[25] Wu, S. Y.; Li, M. R.; Sun, Y. G. *In situ* synchrotron X-ray characterization shining light on the nucleation and growth kinetics of colloidal nanoparticles. *Angew. Chem., Int. Ed.* **2019**, *58*, 8987–8995.
[26] Kim, J.; Ou, Z. H.; Jones, M. R.; Song, X. H.; Chen, Q. Imaging the polymerization of multivalent nanoparticles in solution. *Nat. Commun.* **2017**, *8*, 761.
[27] de Yoreo, J. J.; Gilbert, P. U. P. A.; Sommerdijk, N. A. J. M.; Penn, R. L.; Whitelam, S.; Joester, D.; Zhang, H. Z.; Rimer, J. D.; Navrotsky, A.; Banfield, J. F. et al. Crystallization by particle attachment in synthetic, biogenic, and geologic environments. *Science* **2015**, *349*, aaa6760.
[28] Urban, J. J. Prospects for thermoelectricity in quantum dot hybrid arrays. *Nat. Nanotechnol.* **2015**, *10*, 997–1001.
[29] Liao, H. G.; Zheng, H. Liquid cell transmission electron microscopy. *Annu. Rev. Phys. Chem.* **2016**, *67*, 719–747.
[30] Yuan, W. T.; Zhang, D. W.; Ou, Y.; Fang, K.; Zhu, B. E.; Yang, H. S.; Hansen, T. W.; Wagner, J. B.; Zhang, Z.; Gao, Y. et al. Direct *in situ* tem visualization and insight into the facet-dependent sintering behaviors of gold on TiO_2. *Angew. Chem., Int. Ed.* **2018**, *57*, 16827–16831.
[31] Sutter, E.; Sutter, P.; Tkachenko, A. V.; Krahne, R.; de Graaf, J.; Arciniegas, M.; Manna, L. *In situ* microscopy of the self-assembly of branched nanocrystals in solution. *Nat. Commun.* **2016**, *7*, 11213.
[32] Kim, B. H.; Yang, J.; Lee, D.; Choi, B. K.; Hyeon, T.; Park, J. Liquid-phase transmission electron microscopy for studying colloidal inorganic nanoparticles. *Adv. Mater.* **2018**, *30*, 1703316.
[33] Wang, Y.; Peng, X. X.; Abelson, A.; Xiao, P. H.; Qian, C.; Yu, L.; Ophus, C.; Ercius, P.; Wang, L. W.; Law, M. et al. Dynamic deformability of individual PbSe nanocrystals during superlattice phase transitions. *Sci. Adv.* **2019**, *5*, eaaw5623.
[34] Klokkenburg, M.; Houtepen, A. J.; Koole, R.; de Folter, J. W. J.; Erné, B. H.; van Faassen, E.; Vanmaekelbergh, D. Dipolar structures in colloidal dispersions of PbSe and CdSe quantum dots. *Nano Lett.* **2007**, *7*, 2931–2936.
[35] Yuk, J. M.; Park, J.; Ercius, P.; Kim, K.; Hellebusch, D. J.; Crommie, M. F.; Lee, J. Y.; Zettl, A.; Alivisatos, A. P. High-resolution em of colloidal nanocrystal growth using graphene liquid cells. *Science* **2012**, *336*, 61–64.
[36] Jin, B.; Sushko, M. L.; Liu, Z. M.; Jin, C. H.; Tang, R. K. *In situ* liquid cell tem reveals bridge-induced contact and fusion of au nanocrystals in aqueous solution. *Nano Lett.* **2018**, *18*, 6551–6556.
[37] Anand, U.; Lu, J. Y.; Loh, D.; Aabdin, Z.; Mirsaidov, U. Hydration layer-mediated pairwise interaction of nanoparticles. *Nano Lett.* **2016**, *16*, 786–790.
[38] Zhu, C.; Liang, S. X.; Song, E. H.; Zhou, Y. J.; Wang, W.; Shan, F.; Shi, Y. T.; Hao, C.; Yin, K. B.; Zhang, T. et al. *In-situ* liquid cell transmission electron microscopy investigation on oriented attachment of gold nanoparticles. *Nat. Commun.* **2018**, *9*, 421.
[39] Anderson, N. C.; Hendricks, M. P.; Choi, J. J.; Owen, J. S. Ligand exchange and the stoichiometry of metal chalcogenide nanocrystals: Spectroscopic observation of facile metal-carboxylate displacement and binding. *J. Am. Chem. Soc.* **2013**, *135*, 18536–18548.

Table of contents

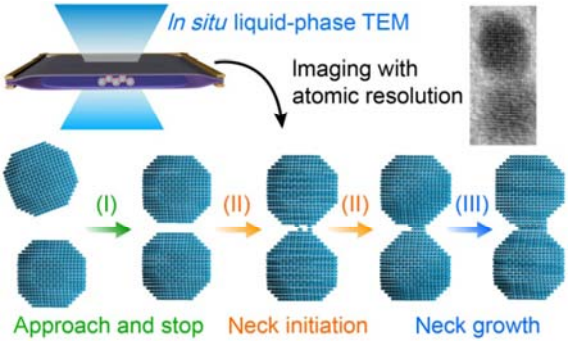

We used *in situ* liquid cell transmission electron microscopy to directly observe the initiation and growth of epitaxial necks between PbSe nanocrystals with atomic details.

Electronic Supplementary Material

In situ TEM observation of neck formation during oriented attachment of PbSe nanocrystals

Yu Wang[1,2], Xinxing Peng[1,3], Alex Abelson[4], Bing-Kai Zhang[1], Caroline Qian[4], Peter Ercius[5], Lin-Wang Wang[1], Matt Law[4], and Haimei Zheng[1,2] (✉)

[1] *Materials Sciences Division, Lawrence Berkeley National Laboratory, Berkeley, California 94720, USA*
[2] *Department of Materials Science and Engineering, University of California, Berkeley, California 94720, USA*
[3] *State Key Lab of Physical Chemistry of Solid Surfaces, Collaborative Innovation Center of Chemistry for Energy Materials, College of Chemistry and Chemical Engineering, Xiamen University, Xiamen 361005, China*
[4] *Department of Chemistry, University of California, Irvine, California 92697, USA*
[5] *National Center for Electron Microscopy, Molecular Foundry, Lawrence Berkeley National Laboratory, Berkeley, California 94720, USA*

Supporting information to https://doi.org/10.1007/s12274-019-2483-8

This PDF file includes:

Supplementary Text
Figures S1 to S4
Captions for Movies S1 to S5
References

Other Supplementary Materials for this manuscript include the following:

Movies S1 to S5

Supplementary Text

Materials

All commercially-available chemicals including oleic acid (OA, tech. grade, 90%), Lead (II) oxide (PbO, 99.9995%, Alfa Aesar), selenium shot (99.999%), trioctylphosphine (TOP, tech. grade, >97%, Strem Chemicals Inc.), 1-octadecene (ODE, 90%, Aldrich), diphenylphosphine (DPP, 98%, Aldrich), hexane (anhydrous, 99%, Sigma-Aldrich), ethylene glycol (EG, anhydrous, 99.8%, Sigma-Aldrich), and ethyl alcohol (anhydrous, 99.5%, Sigma-Aldrich) were used as received. Ultra-thin carbon film (10 nm, 400 mesh) supported copper grids were purchased from Electron Microscopy Sciences (EMS).

Synthesis of PbSe nanocrystals

PbSe nanocrystals were synthesized and purified as previously reported [S1] in a nitrogen-filled glove box with oxygen content less than 10 ppm. Typically, 1.50 g PbO, 5.0 g OA, and 10.0 g ODE were thoroughly degassed and heated to 180 °C under flowing argon, then 9.5 mL of a 1 M solution of TOP-Se containing 0.20 mL DPP was quickly injected to start the nucleation. After a growth of 105 ± 3 s, the reaction was quenched by a liquid nitrogen bath, gradually warmed to 35 °C and diluted with 10 mL anhydrous hexane. The nanocrystal product was washed three times using ethanol/hexane, dried completely.

TEM characterization

In ex situ experiments, hexagonal monolayers of PbSe nanocrystals were self-assembled through the evaporation of 4 μL of a 0.5 mg/mL hexane suspension of the nanocrystals on a 10-nm thick carbon-film TEM grid. To prepare the square superlattice, a hexagonal monolayer on a carbon-film TEM grid was immersed in anhydrous EG for 30 sec to trigger the oriented attachment. The samples of hexagonal monolayer or square superlattices were dried completely in vacuum before the HAADF-STEM characterizations, which were performed using the probe aberration-corrected Thermo Fischer (formerly FEI) Titan 80-300 named TEAM I at the Molecular Foundry (MF), Lawrence Berkeley National Laboratory (LBNL).

In situ experiments were started from the dried hexagonal monolayers of PbSe nanocrystals that were formed through the same evaporation method used for ex situ experiments. We then deposited 100 nL of anhydrous EG (or 100 nL of 15 mM EDA solution in EG in the comparison experiment) on a second TEM grid and sandwiched the two grids together to form a carbon-film liquid cell. Before loading the PbSe NCs and EG, the carbon-film TEM grids were pretreated with oxygen/argon plasma for 30 s to increase the wetting of EG solution on the carbon film and improve the seal of the liquid cell. The liquid cell was installed in a TEM holder (all under nitrogen atmosphere), which was then quickly removed from the glove box and inserted into the TEM. In situ imaging was performed using JEOL 2100 TEM at Materials Science Division, LBNL. The microscope, operating voltage and electron beam intensity for each experiment are indicated in the corresponding movie captions.

Address correspondence to hmzheng@lbl.gov

Computer vision of TEM and STEM images

The PbSe nanocrystals used in this study have a near-spherical truncated cuboctahedra structure. We have reported a method based on Laplacian of the Gaussian (LoG) filter to recognize spherical nanoparticles in TEM images [S2]. Here, we perform the recognition of nanocrystals in TEM movies through the same LoG method. The gap distances between neighboring nanocrystals (shown in Figs. 1D, S1C, and S2C) are evaluated by subtracting the center-to-center distance by the crystal radiuses of two nanocrystals. When two nanocrystals stop approaching and start the neck initiation, the gap distance becomes settled and the stop points in Figs. 1D, S1C, and S2C are determined manually when a clear neck forms between the two nanocrystals. Alternatively, movie S4 and Fig. 2A have the atomic resolution, allowing us to count the neck dimension directly in atomic layers, as shown by the right axial of Fig. 2C. As we know the viewing zone axial is close to [100] from Fig. 2A, we can convert the neck width from atomic layers into nanometric scale, i.e., one atomic layer equals to 0.3 nm.

We used a similar method to analyze the center position and diameter of nanocrystals in the STEM image in Fig. S3A. We generate LoG filters with varying diameters and convolve STEM images with the filters to produce strong signal at the center of nanocrystals. When the LoG filter has a same radius as a nanocrystal, it results in the highest intensity in the convolved image. Therefore, by varying the diameter of LoG filters, we obtain the best fitting of each nanocrystal with their center positions and diameters. Red circles with the fitted center positions and diameters are drawn to show how accurate the recognitions are (Fig. S3A).

To determine whether two neighboring nanocrystals are connected (by neck), the brightness at the middle point of two nanocrystal is compared with a threshold that is evaluated by the image histogram in the local area. If the two nanocrystals are connected, a blue line would be drawn to connect their centers (as shown in Fig. S3B). To determine the neck widths, virtual lines are drawn at the middle points of neighboring nanocrystals and along the perpendicular direction of the blue lines, brightness along the virtual lines is compared with another threshold that is evaluated by the image histogram in the neck area. The determine neck widths are shown by the green lines as shown in Fig. S3B.

Density functional theory calculations

The density functional theory (DFT) calculations were performed using the Vienna ab initio simulation package (VASP) [S3], within the projector augmented-wave formalism. The exchange-correlation interaction is described by generalized gradient approximation (GGA) with the Perdew–Burke–Ernzerhof (PBE) functional [S4]. Van der Waals interaction was described by using the empirical correction in Grimme's scheme, i.e. DFT+D3 [S5]. A cutoff energy of 500 eV and a 3 × 3 × 2 Monkhorst-Pack k-point mesh was used for all simulations. We have employed the DFT ground state structure containing two slabs of four-layer rock-salt PdSe crystals with a varying spacing as the parent structure (Fig. 4A). An oleic acid fragment (without the alkyl tail after the alkene group) was placed in the gap of the double-slab structure and attached to one {001} PbSe facet through a Pb-O coordination bond. In our geometry optimizations, all atoms are fully relaxed until all force components acting on the atoms are below 0.005 eV/Å. System energies are calculated with varying gap distances between the two slabs.

The critical nucleus size was evaluated by adding pairs of Pb and Se atoms into a two-atom-long gap of the double-slab structure (Fig. 4B). The energy change as atoms are moved from bulk into the gap are calculated by following equation:

$$\Delta E = E_{\text{necked}} - (E_{\text{double-slab}} + n \times E_{\text{bulk}})$$

where the E_{necked} is the total energy of the double-slab structure with added neck, $E_{double\text{-}slab}$ is the energy of the double-slab structure with two-atom-long empty gap, n is the number of Pb-Se pairs added into the gap, and E_{bulk} is the energy of a pair of Pb and Se in PbSe bulk form. The two-atom-long edge-to-edge distance between the two slabs were kept consistent when adding Pb-Se pairs. The Pb-Se pairs were added epitaxially to follow the rock-salt structure of PbSe and packed closely in the gap to reduce the surface energy. The relationship between ΔE and the number of added Pb-Se pairs are shown in Fig. 4D.

Supplementary Figures

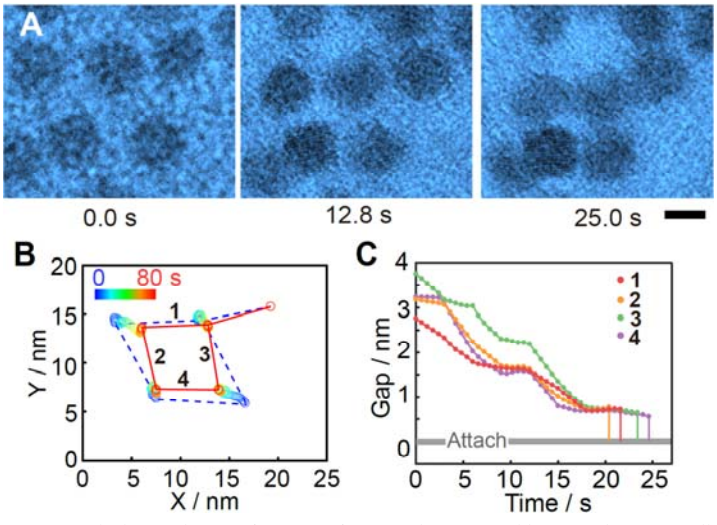

Figure S1 Neck formation between PbSe nanocrystals during the transformation from an oleate-capped hexagonal to epitaxially-connected square assembly. (A) Sequence of in situ TEM images showing the translational motion and necking of five nanocrystals. Images are extracted from Movie S2 and shown in false color. Scale bar, 5 nm. (B) Trajectories of the nanocrystal centers showing the transformation from the hexagonal to square geometry. Dashed and solid lines denote nanocrystal pairs that are unconnected or epitaxially connected, respectively. (C) Time trace of the gap distances showing the three-stage necking pathway. Colored vertical lines connected to the gray (attach) bar denote that a stable nucleus forms between the respective nanocrystal pair.

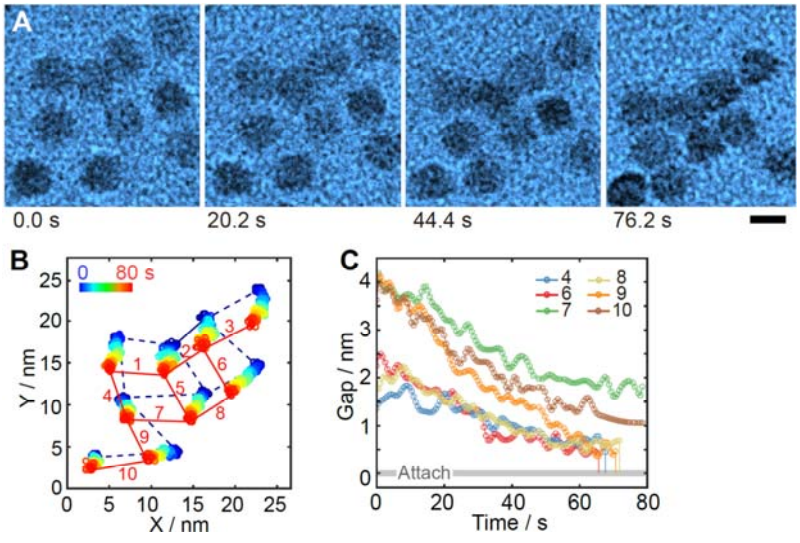

Figure S2 Neck formation between PbSe nanocrystals during the transformation from an oleate-capped hexagonal to epitaxially-connected square assembly. (A) Sequence of in situ TEM images showing the translational motion and necking of 9 nanocrystals. Images are extracted from Movie S3 and shown in false color. Scale bar, 5 nm. (B) Trajectories of the nanocrystal centers showing the transformation from the hexagonal to square geometry. Dashed and solid lines denote nanocrystal pairs that are unconnected or epitaxially connected, respectively. (C) Time trace of the gap distances of six nanocrystal pairs showing the three-stage necking pathway. Colored vertical lines connected to the gray (attach) bar denote that a stable nucleus forms between the respective nanocrystal pair.

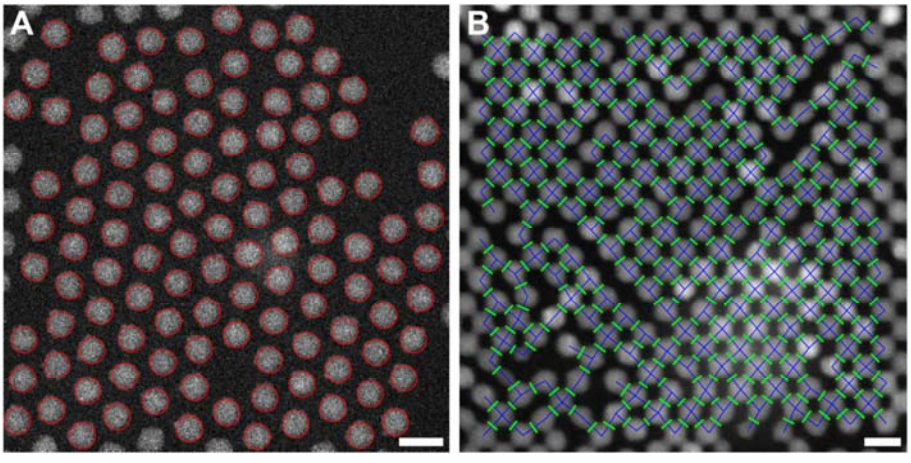

Figure S3 Computer vision on the ex situ STEM images of large-area superlattices. Both scale bars are 10 nm. (A) Nanocrystals in a hexagonal oleate-capped monolayer are fitted as spherical objects. The position and diameter of each nanocrystal are obtained using a disk-fitting method (see supplementary text for details). Best fitted results are shown with red circles. (B) Inter-nanocrystal connectivity and the neck widths are recognized based on the brightness in the neck area (see supplementary text for details). Blue and green lines show the center-to-center distance and neck width between connected nanocrystals.

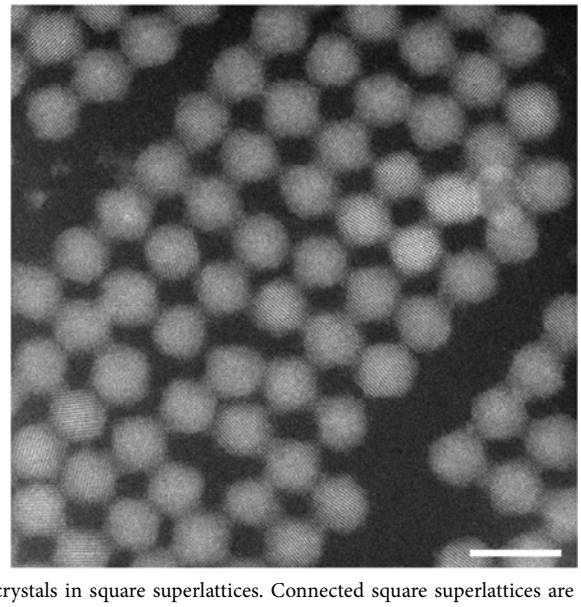

Figure S4 Epitaxial connection between nanocrystals in square superlattices. Connected square superlattices are formed ex situ by immersing a carbon-film grid loaded with hexagonal monolayers of nanocrystals into EG solvent for 10 seconds.

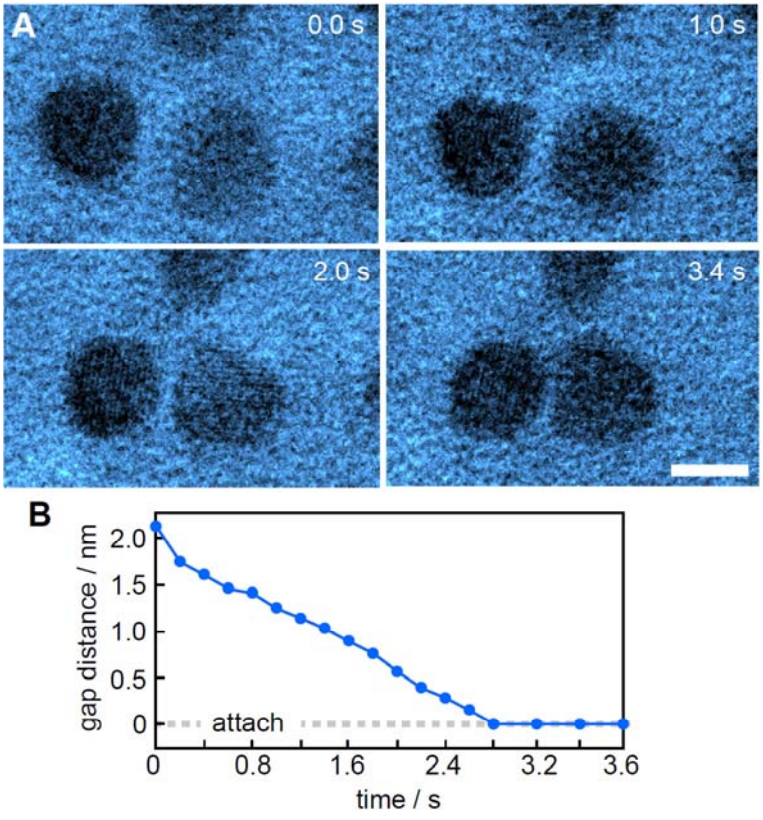

Figure S5 Direct attachment of two PbSe nanocrystals in EDA solution. (A) Sequence of in situ TEM images showing the translational motion of two nanocrystals. Images are extracted from Movie S5 and shown in false color. Scale bar, 5 nm. (B) Time trace of the gap distances showing the direct attachment of two nanocrystals, different from the neck formation that is observed in pure EG experiments.

Movie Captions

Movie S1 In situ liquid phase TEM movie showing the neck formation between PbSe nanocrystals during the transformation from an oleate-capped hexagonal to epitaxially-connected square assembly. Analysis is shown in Fig. 1. Movie was recorded using JEOL 2100 TEM under 200 keV with an electron beam current of ~700 electrons $Å^{-2}$ s^{-1}.

Movie S2 In situ liquid phase TEM movie showing the neck formation between PbSe nanocrystals during the transformation from an oleate-capped hexagonal to epitaxially-connected square assembly. Analysis is shown in Fig. S1. Movie was recorded using JEOL 2100 TEM under 200 keV with an electron beam current of ~700 electrons $Å^{-2}$ s^{-1}.

Movie S3 In situ liquid phase TEM movie showing the neck formation between PbSe nanocrystals during the transformation from an oleate-capped hexagonal to epitaxially-connected square assembly. Analysis is shown in Fig. S2. Movie was recorded using JEOL 2100 TEM under 200 keV with an electron beam current of ~700 electrons $Å^{-2}$ s^{-1}.

Movie S4 In situ liquid phase TEM movie showing the atomistic pathway of neck initiation between two PbSe nanocrystals. Analysis is shown in Fig. 2. Movie was recorded using JEOL 2100 TEM under 200 keV with an electron beam current of ~700 electrons $Å^{-2}$ s^{-1}.

Movie S5 In situ liquid phase TEM movie showing the direct attachment of two PbSe nanocrystals in EDA solution. Analysis is shown in Fig. S4. Movie was recorded using JEOL 2100 TEM under 200 keV with an electron beam current of ~700 electrons $Å^{-2}$ s^{-1}.

References

[S1] X. Peng, A. Abelson, Y. Wang, C. Qian, J. Shangguan, Q. Zhang, L. Yu, Z.-W. Yin, W. Zheng, K. C. Bustillo, X. Guo, H.-G. Liao, S.-G. Sun, M. Law, H. Zheng, *Chem. Mater.* **2019**, *31*, 190-199.

[S2] A. S. Powers, H.-G. Liao, S. N. Raja, N. D. Bronstein, A. P. Alivisatos, H. Zheng, *Nano Lett.* **2017**, *17*, 15-20.

[S3] a) G. Kresse, J. Furthmüller, *Comput. Mater. Sci.* **1996**, *6*, 15-50; b) G. Kresse, J. Furthmüller, *Phys. Rev. B* **1996**, *54*, 11169-11186.

[S4] J. P. Perdew, K. Burke, M. Ernzerhof, *Phys. Rev. Lett.* **1996**, *77*, 3865-3868.

[S5] S. Grimme, *J. Computat. Chem.* **2006**, *27*, 1787-1799.